**Adaptive Optics for Extremely Large Telescopes 4 – Conference Proceedings**

**Title**
Measuring Segment Piston with a Non-Redundant Pupil Mask on the Giant Magellan Telescope

**Permalink**
https://escholarship.org/uc/item/62p140z1

**Journal**
Adaptive Optics for Extremely Large Telescopes 4 – Conference Proceedings, 1(1)

**Authors**
van Dam, Marcos
Tuthill, Peter
Cheetham, Anthony

**Publication Date**
2015

**DOI**
10.20353/K3T4CP1131559

**Copyright Information**

Peer reviewed

# Measuring Segment Piston with a Non-Redundant Pupil Mask on the Giant Magellan Telescope

Marcos A. van Dam,[a] Peter G. Tuthill[b], Anthony C. Cheetham,[b,c] and Fernando Quiros-Pacheco[d]

[a]Flat Wavefronts, 21 Lascelles Street, Christchurch 8022, New Zealand;
[b]School of Physics, University of Sydney, NSW 2006, Australia;
[c]Department of Astronomy, University of Geneva, 24, Rue General Dufour, 1211 Geneva 4, Switzerland;
[d]Giant Magellan Telescope Observatory Corporation, P.O. Box 90933, Pasadena, CA 91109, USA

## ABSTRACT

The Giant Magellan Telescope (GMT) consists of seven 8.365 m segments with a separation of 0.345 m. A unique challenge for GMT lies in phasing these segments and, in particular, how to measure segment piston optically. In this paper, we present a results of a phasing strategy using a non-redundant pupil mask. We show how this method can be extended to measure segment piston differences of more than half a wave by using broadband light.

**Keywords:** non-redundant masks, phasing, Giant Magellan Telescope, adaptive optics, simulations

## 1. INTRODUCTION

The Giant Magellan Telescope (GMT) consists of seven 8.365 m segments with a separation of 0.345 m. A unique challenge for GMT lies in phasing these segments and, in particular, how to measure segment piston optically. In order to image at the diffraction limit of the telescope (equivalent to a diameter of approximately 25.4 m), it is crucial to phase the primary and secondary mirrors to a fraction of the imaging wavelength. There are two planned diffraction-limited adaptive optics (AO) modes for the GMT, which require a phased telescope.[1] A natural guide star adaptive optics (NGS AO) system with a visible light pyramid wavefront sensor is used when there is a sufficiently bright star near the science target. For greater sky coverage, there is also a laser tomography adaptive optics (LTAO) system that employs six side-projected laser guide stars, along with a single natural guide star to measure tip-tilt. This tip-tilt star can be much fainter and further away from the science target than the star used NGS AO. The proposed solution to the telescope optical phasing problem is addressed elsewhere.[2,3]

In addition to telescope segment piston, adaptive optics (AO) corrected observations using the GMT will suffer from atmospheric segment piston. Atmospheric segment piston is the error in estimating the segment piston component of the atmospheric wavefront. The Shack-Hartmann WFS (SHWFS) does not measure discontinuities in the wavefront. As a consequence, the reconstructed wavefront is the smoothest wavefront consistent with the wavefront slope measurements. The difference between the true wavefront and the wavefront reconstructed from wavefront slope measurements is of the order of 100 nm for an LTAO system and 150 nm for a SHWFS based NGS AO system.[4]

The GMT NGS AO system will use a pyramid wavefront sensor (PWFS) to measure the wavefront. The PWFS has been shown to be more sensitive than the SHWFS. Another nice property of the PWFS is the ability to measure phase differences,[5] which makes it ideal for a segment telescope like the GMT. The ability to sense segment piston with a PWFS is limited by two factors. First, any segment phase errors of greater than half a wave will alias into an incorrect measurement due to the well known $2\pi$ phase ambiguity. Second, in the presence of residual wavefront errors, the sensitivity of the segment piston measurement degrades significantly.

The residual aberrations can stem from worse than average seeing or from strong windshake which not only shakes the whole telescope, but makes the individual segments shake independently of each other. As a result, the segment piston measurements from the PWFS can lead to a wavefront reconstruction where one or more segments have an incorrect value by an integer number of wavelengths. The baseline solution is to use a second channel with a second PWFS at a different wavelength and to use the wavelength diversity to disentangle the phase jumps.[6]

In this report, we investigate a different technique to measure segment piston problem based on a non-redundant aperture mask. This technique, called Fizeau interferometric cophasing of segmented mirrors (FICSM), was used in simulations of the JWST[7] and in laboratory studies[8] by Cheetham et al to measure tip-tilt and phase errors.

In Section 2, we explain how the FICSM sensor works. We show in Section 3 that, by using broadband light, we can overcome the $2\pi$ ambiguity inherent in interferometric methods and make segment piston measurements of several waves. Numerical simulation results are presented in Section 4, followed by conclusions in Section 5.

## 2. NARROWBAND FICSM

A non-redundant aperture mask is a pupil mask with a number of circular holes. The light from the different holes interferes and the resulting image can be used to estimate the difference in phase between the holes. By judicious selection of the location of the holes, each pair of holes has a different baseline and each baseline can be unambiguously extracted from the image at the focal plane. To be strictly non-redundant, the hole diameter must be less than or equal to half the shortest baseline. When using broadband light, the size of the holes must be decreased to avoid the baselines overlapping in Fourier space. The pupil mask used in this report, with one hole per segment, is reproduced in Fig. 1. The holes in the mask have a diameter of 2.5 m when using narrowband and 2.0 m when using broadband light. Let us consider a flat wavefront with a single poked segment
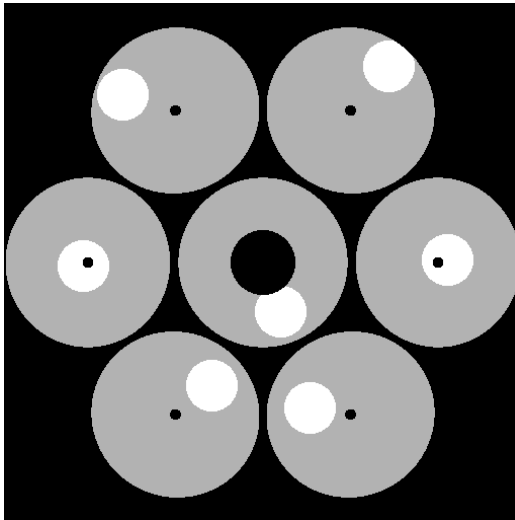


Figure 1: The non-redundant pupil mask used in this paper. The gray area is the telescope pupil, while the white circles represent the holes in the pupil mask.

imaged through the non-redundant pupil mask, as shown in Fig. 2. We take the Fourier transform of the image and extract its phase, a quantity we call the "Fourier phase" (Fig. 2). There are 42 measurements, but only 21 are independent, since the other 21 phase estimates are identical but with a negative sign. The six measurements that show a positive phase correspond to the phase difference between the poked segments and each of the six poked segments. The other measurements, which compare the unpoked segments, are all zero.

Mathematically, the phase is estimated from an image, $I$, in two steps. First, we find the Fourier phase, $\theta(u, v)$ according to:

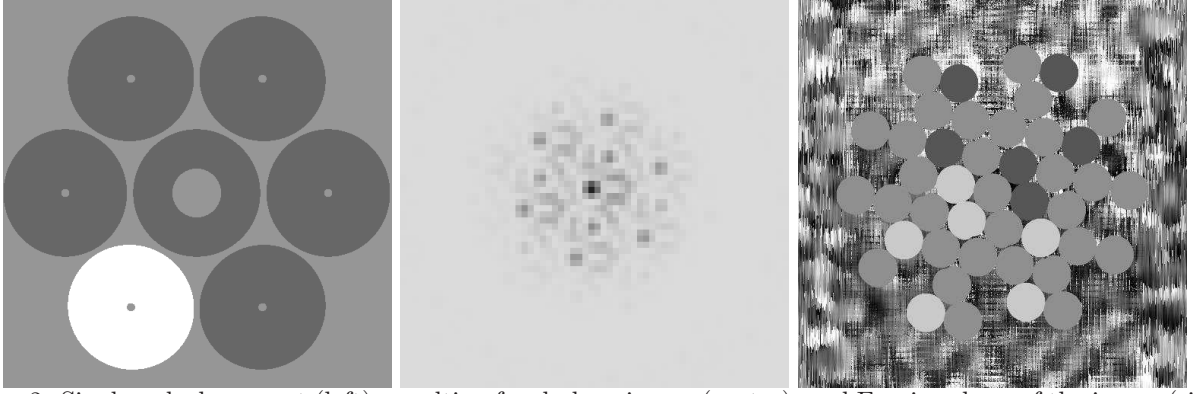$$\theta(u, v) = \arg\{F\{I(x, y)\}\}, \tag{1}$$

Figure 2: Single poked segment (left), resulting focal plane image (center), and Fourier phase of the image (right) using monochromatic light.

where $F\{\}$ denotes the Fourier transform and $\arg\{\}$ is the phase of the complex quantity. Then the phase difference between holes $k$ and $l$, $\phi_{kl}$ is estimated by integrating the Fourier phase over the circular area in the Fourier plane, $P_{kl}$, that corresponds to the baselines between holes $k$ and $l$:

$$\hat{\phi}_{kl} = \frac{\int P_{kl}(u,v)\theta(u,v)}{P_{kl}(u,v)}. \tag{2}$$

In the absence of any wavefront aberrations, the phase measurements are completely linear, and segment piston can be reconstructed up to half a wavelength, as shown in Fig. 3. This algorithm also works with broadband
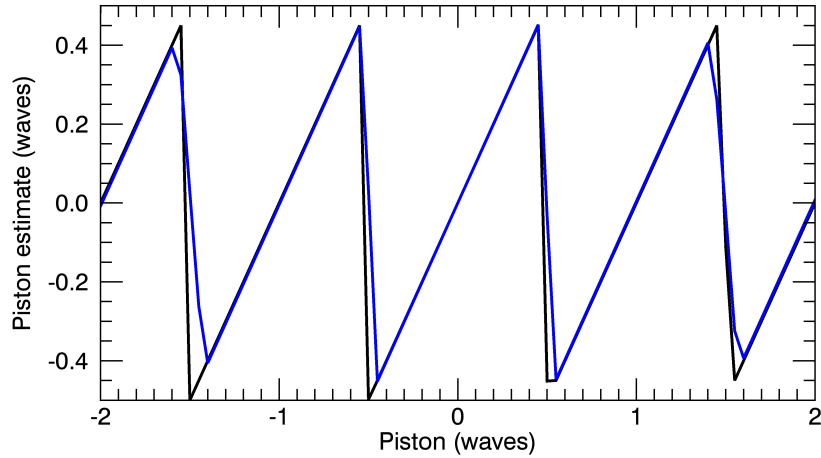


Figure 3: Response of the phase sensor to different poke amplitudes for narrowband light (black) and a filter with a 20% bandwidth (blue).

light. In these simulations, we model broadband light as a top-hat function with a passband of 20% of the central wavelength. Nine discrete wavelengths are used to emulate the broadband behavior. Resulting images and the Fourier phase using broadband light are shown in Fig. 4. In practice, we use only a limited region of the image, in order to limit the noise, as shown in Fig. 5. At distances far from the center of the image, the noise dominates the signal. In addition, the information present in the images far from the center corresponds to high spatial frequencies from atmospheric turbulence and not information about the piston difference between the holes. To filter this high frequency information, the image is windowed. In our studies, two types of windows are used: a hard circular window and a super Gaussian window. The hard window takes values of 1 inside the
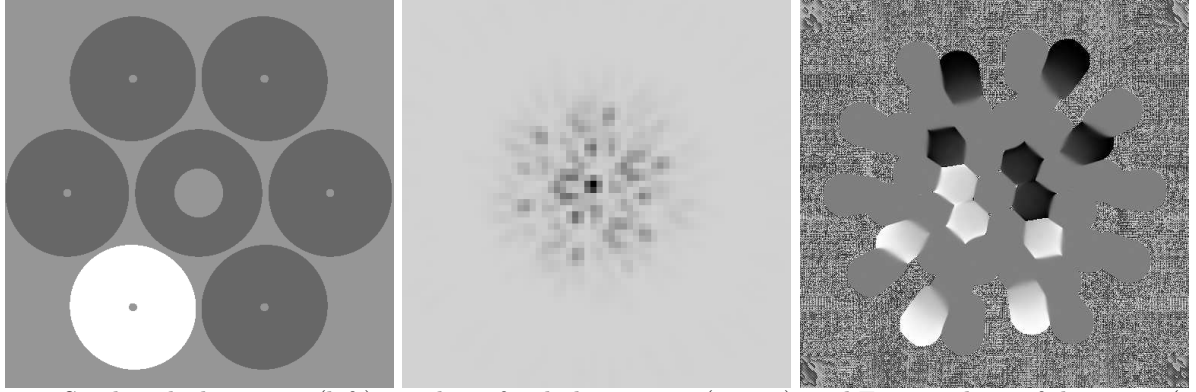
Figure 4: Single poked segment (left), resulting focal plane image (center), and Fourier phase of the image (right) using broadband light.

window and 0 elsewhere, while the super Gaussian window has an intensity that goes as $\exp[-r^4]$, where $r$ is the radial distance from the center of the window. We find that that narrowband algorithm works better with hard windows, while the broadband algorithm behaves better with a soft window. The optimal window diameter, used in the simulations, is $0.1''$ for a wavelength of $0.8\,\mu\mathrm{m}$, as shown in Fig. 5, and $0.25''$ at $2.2\,\mu\mathrm{m}$.
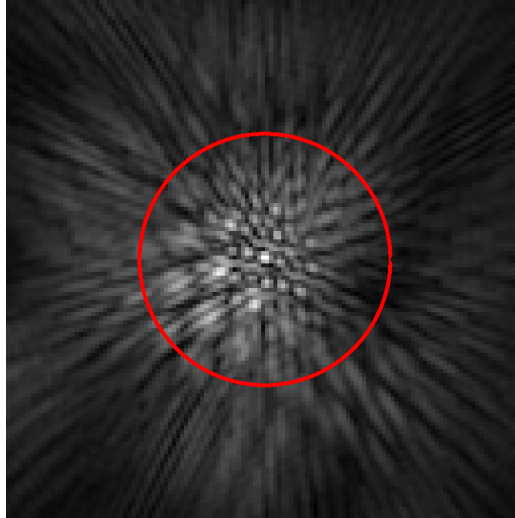


Figure 5: Typical FICSM image with a square root stretch at $0.8\,\mu\mathrm{m}$ with $r_0$ of $0.15\,\mathrm{m}$. The $0.1''$ diameter extent window is shown in red.

The estimate of the phase difference between two holes is found by averaging the Fourier phase over a region, as seen in Eq. (2). For monochromatic light, a region corresponding to twice the diameter of the hole can be used to incorporate all of the baselines. However, using a smaller integration area gives more accurate results, and the optimal diameter for $P_{kl}$ is 1.5 times the hole diameter.

An even more interesting result is that using a single Fourier phase point at the center of $P_{kl}$ leads to phase estimates almost as good as using the much larger integration area. By using a single point, we eliminate issues related to phase wrapping of the Fourier phase. As an example, consider Fig. 6, where one of the segments has been poked by half a wave. For regions in the Fourier plane where the phase is wrapped, the phase estimate will lie at at an unpredictable value somewhere between $\pm\lambda/2$. If, instead, we use the center baseline to estimate the phase, then the estimated phase will be very close to either $-\lambda/2$ or $\lambda/2$. Alternatively, a phase unwrapping routine could be applied to the Fourier phase before integrating over the corresponding region, $P_{kl}$.

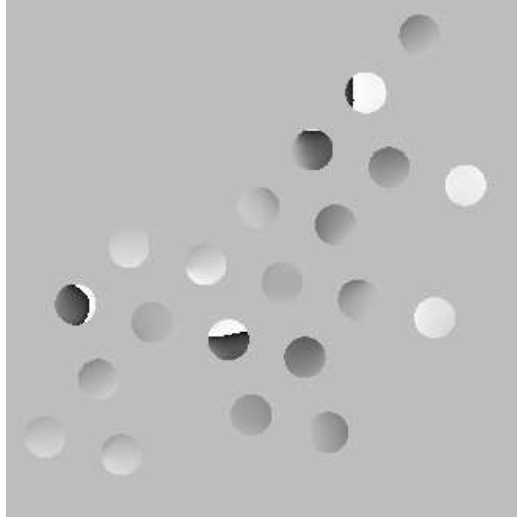An alternative approach to reconstructing the phase from the FICSM images is to use a phase retrieval

Figure 6: Phase wrapping of the Fourier phase over the integration regions.

algorithm, such as the Gerchberg-Saxton algorithm.[9] Because of the non-redundancy of the information in the images, the convergence is very fast and does not appear to stagnate.

## 3. BROADBAND FICSM

When using the the narrowband algorithm (regardless of whether the passband is narrow or broad), we are limited in capture range to half a wave before the measurement wraps, as seen in Fig. 3. The broadband phasing algorithm, designed to increase the dynamic range of the sensor, takes advantage of the fact that a broadband measurement of the segment piston error has a wavelength dependent signature. If we poke a segment by varying amounts, we notice that the Fourier phase is not constant over the area of integration, but contains a tilt. This is caused by the fact that the fringes corresponding to the long wavelength end of the filter are further from the center of the image, and have a lower phase (since the piston is a smaller fraction of the wavelength). The way that the phase varies across the Fourier plane is illustrated in Figs. 7 and 8.
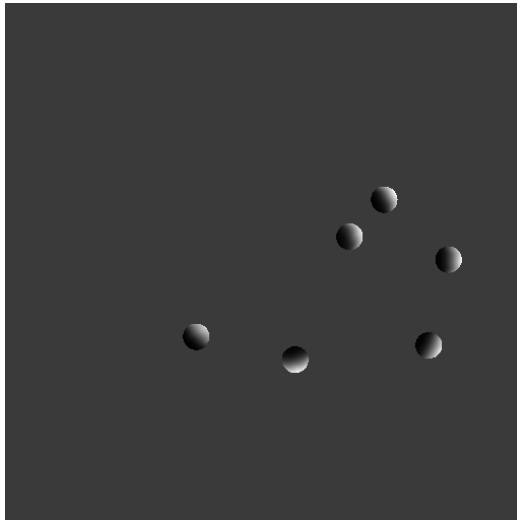


Figure 7: The Fourier phase of the a broadband image for a segment poked by four waves..

In the original paper,[7] Cheetham *et al.* suggests using a Chi-squared fit of the measured phase to a precomputed to determine the phase to within a wave. In our application, this is trickier because of the presence of
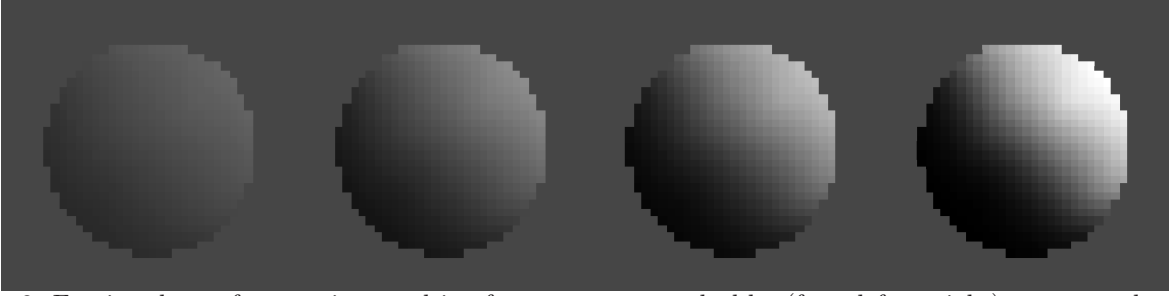
Figure 8: Fourier phase of one region resulting from a segment poked by (from left to right) one, two, three and four waves.

random and unknown residual atmospheric turbulence.

A segment piston causes a linear tilt in the Fourier phase. Due to phase wrapping, the Fourier phase often incurs phase jumps over $P_{kl}$, so trying to fit tip-tilt directly to the Fourier phase does not work.

The estimate of the phase difference between holes $k$ and $l$ is as follows. First, we obtain the Fourier phase of the image, $\theta(u,v)$, as in the narrowband case. We wish to find the slope of Fourier phase over the integration region, $P_{kl}$ (*e.g.*, the integration region shown in Fig. 8). By analogy with the SHWFS, we consider $\theta(u,v)$ to be the phase of a wavefront and propagate this into the image plane to obtain the intensity of the spot, $U_{kl}(x,y)$:

$$U_{kl}(x,y) = |F\{P_{kl}\exp[i\theta(u,v)]\}|^2. \tag{3}$$

We take advantage of the fact that a tilt in the phase leads to a displacement of an image irrespective of any discontinuity in the phase. Finally, we calculate the center-of-gravity of the spot, $U_{kl}(x,y)$ in the direction between the two holes. We denote this center-of-gravity operator as $G\{\}$. The phase difference between holes $k$ and $l$ is proportional to the center-of-gravity of the spot:

$$\hat{\phi}_{kl} \propto G\{U_{kl}(x,y)\} \tag{4}$$

The proportionality constant is calculated by poking the segments and measuring the motion of the spot.

Any wavefront tip-tilt over the extent of the hole will also give rise to a similar signal (i.e., a linearly varying $\theta(u,v)$). From a single measurement of the slope of the Fourier phase, it is not possible to tell whether the signal is caused by a piston error or a tip-tilt error. However, the signal can be disentangled using all the measurements, since there are 42 measurements (21 measurements of the tip-tilt of the Fourier phase) and 21 unknowns (seven piston values and fourteen tip-tilt values). A least-squares reconstructor is used to convert the slope estimates into piston and segment tip-tilt estimates.

The response of the sensor is approximately linear over a wide capture range of several waves, as can be seen in Fig. 9.

## 4. SIMULATION RESULTS

### 4.1 Simulation description

In order to understand the performance of the FICSM sensor, numerical simulations were run in YAO, a general purpose end-to-end simulation tool written in the yorick language.[10] Two applications were considered. First, a pupil mask can be included in a science instrument such as GMTIFS, the GMT's first-light AO-corrected imager and spectrograph. From this, we can determine whether the telescope is correctly phased or not, but unfortunately not while science data is being captured. The second application is to correct for atmospheric segment piston while running the NGS AO system. The segment piston measurement from the FICSM sensor can be used to correct the segment piston instead of the measurements from the PWFS, or it can be used to determine whether the PWFS has led to a jump of one or more waves in a given segment.

The atmospheric parameters are derived from the typical-typical profile for January 2008 from Goodwin[11] and are reproduced in Table 1 for convenience. The value of $r_0$ is 0.151 m at a wavelength of 500 nm. An outer scale of 60 m is assumed.
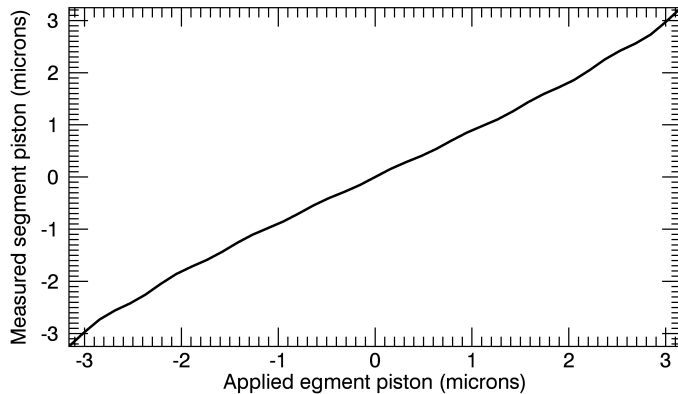
Figure 9: Response of the broadband phase sensor to different poke amplitudes at 0.8 μm with a flat input wavefront.

Table 1: Turbulence profile used in the simulations

| Elevation (m) | Turbulence fraction | Wind speed ($\mathrm{m\,s^{-1}}$) | Wind direction (°) |
|---|---|---|---|
| 25 | 0.126 | 5.65 | 0.78 |
| 275 | 0.087 | 5.80 | 8.25 |
| 425 | 0.067 | 5.89 | 12.48 |
| 1250 | 0.350 | 6.64 | 32.50 |
| 4000 | 0.227 | 13.29 | 72.10 |
| 8000 | 0.068 | 34.83 | 93.20 |
| 13000 | 0.075 | 29.42 | 100.05 |

## 4.2 Measuring telescope segment piston using the science camera

In this application, we measure the segment piston error as seen by the science camera. GMTIFS uses a Hawaii-4RG infrared detector with on-detector guide windows. These on-detector guide windows can be read faster and with a lower read noise than reading out the whole array. The noise characteristics of the detector and the associated photometric parameters used in the simulations are tabulated in Table 2.

Table 2: Photometric parameters used in the simulations of the FICSM sensor inside GMTIFS.

| | |
|---|---|
| Central wavelength | 2.179 μm |
| Photometric zero point | $7.0 \times 10^{11}$ |
| Sky background (magnitude per arcsec$^2$) | 13.4 |
| Optical throughput | 55% |
| Quantum efficiency | 85% |
| Noise excess factor | 1 |
| Read noise | $3e^-$ |
| Dark current | $0e^-$ |

We are interested to see how well the FICSM sensor can measure segment piston when the LTAO system is in operation. For simplicity, we replaced the LTAO system by a SHWFS-based NGS AO system with a single guide star. Residual wavefronts were generated by simulating a $50 \times 50$ SHWFS running at 500 Hz. This gives a residual wavefront of 240 nm RMS, which is what we expect from the LTAO system. In addition, 200 nm of random segment piston error was added to the wavefronts, and it is this segment piston which we would like to measure.

The FICSM sensor operates at K-band, with 1 s exposures. The simulations as a function of guide star

magnitude are plotted in Fig. 10. It can be seen that the limiting magnitude of the narrowband algorithm is
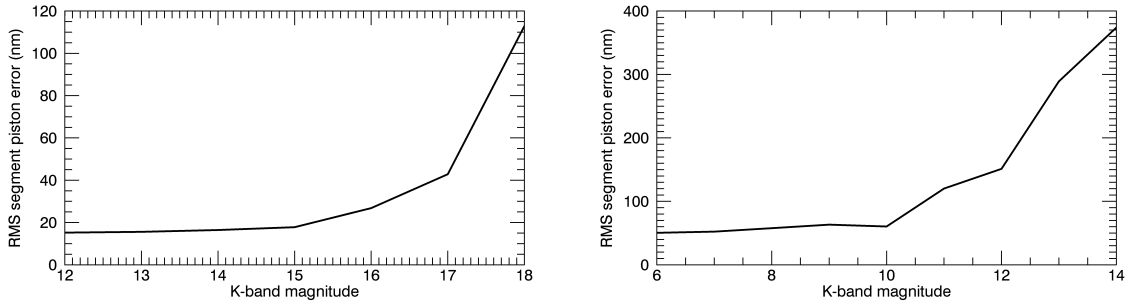


Figure 10: RMS segment piston error as a function of K-band guide star magnitude using the narrowband (left) and broadband (right) FICSM sensor behind the LTAO system.

about $m_K = 17$ for 1 s integrations, and equally good results could be obtained with fainter stars by increasing the exposure time. The simulations were repeated using the broadband piston sensor, which would be needed in the unlikely case that the telescope phasing error is greater than 1 μm. The broadband sensor needs to estimate the segment piston to within half a wave, at which point the narrowband algorithm can take over. The limiting magnitude in this case is about $m_K = 14$ for 1 s exposures.

## 4.3 Measuring atmospheric segment piston behind the pyramid wavefront sensor

As previously mentioned, the PWFS can measure segment piston at fast frame rates, but it can suffer from phase jumps due to the $2\pi$ phase jump problem. There are two ways to resolve this: using a second measurement at a different wavelength, or using broadband light.

First, we consider measuring segment piston at a second wavelength, $\lambda_2$. If we assume that the PWFS channel drives the segment piston error measurement, $p(\lambda_1)$ to zero, then the estimate of the true segment piston based on a measurement at a second wavelength is

$$\hat{p} = p(\lambda_2)\frac{\lambda_1}{\lambda_2 - \lambda_1}. \tag{5}$$

In this study, $\lambda_1$=0.75 μm and $\lambda_1$=0.85 μm. In order to estimate $\hat{p}$ to within half a wave, the accuracy of the second measurement needs to be less than 40 nm. Second, we measure segment piston using the broadband FICSM sensor. Here, measuring to 300 nm provides sufficient accuracy. In both cases, the measurements are made at a rate of 10 Hz, using only 10% of the available light (the rest is passed to the PWFS).The photometric and noise parameters are tabulated in Table 3.

Table 3: Photometric parameters used in the simulations of the FICSM sensor behind the pyramid sensor.

| Passband | Monochromatic | Broadband |
|---|---|---|
| Central wavelength | 0.850 μm | 0.750 μm |
| Photometric zero point | $0.90\times10^{12}$ | $6.7\times10^{12}$ |
| Sky background (magnitude per arcsec$^2$) | 18.5 | 18.5 |
| Optical throughput | 5.5% | 5.5% |
| Quantum efficiency | 85% | 85% |
| Noise excess factor | 1.41 | 1.41 |
| Read noise | $0.5e^-$ | $0.5e^-$ |
| Dark current | $0e^-$ | $0e^-$ |

The wavefront corrected by the PWFS was obtained via simulation in PASSATA, an IDL-based Monte-Carlo simulation tool written specifically to simulate the performance of pyramid sensors. 6 s of simulation data was
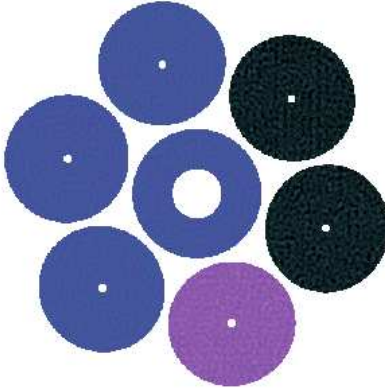
Figure 11: Example of the residual wavefront produced by the pyramid sensor.

generated, and the data used corresponded to the case where the correction had converged, but three segments had been "ejected", as can be seen in Fig. 11. The PWFS has $92 \times 92$ subapertures and runs at 1 kHz, leading to excellent correction with an RMS residual wavefront of 80 nm excluding segment piston errors.
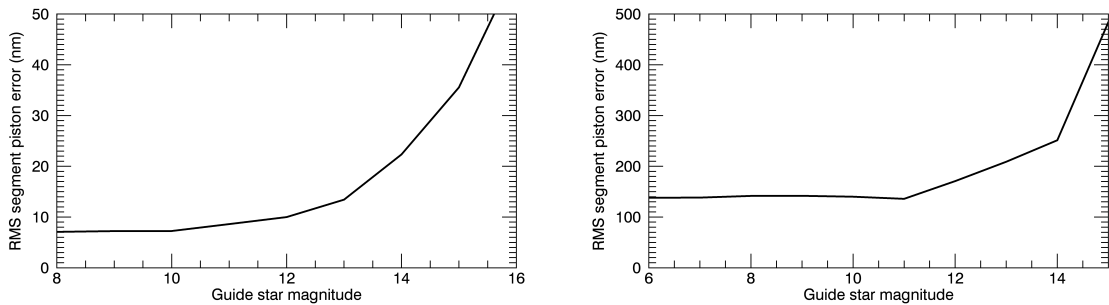
The results are plotted in Fig. 12.



Figure 12: RMS segment piston error as a function of I-band guide star magnitude using the narrowband (left) and broadband (right) FICSM sensor behind a PWFS.

## 5. CONCLUSION

In this paper, we evaluate the performance of FICSM to measuring segment piston on the GMT. This technique uses a non-redundant pupil mask and an imaging camera. From the Fourier phase of the images, we are able to measure segment piston unambiguously using both monochromatic and broadband light. When imaging in broadband light, we can take advantage of the wavelength-dependent signature in the Fourier phase to extend the capture range beyond the half a wave restriction imposed by all direct interferometric measurements.

Simulations were run to test the performance for two different cases. First, a pupil mask was inserted into the science instrument, and K-band images were produced. From 1 s integrations, we can measure segment piston down to 40 nm with an $m_K = 17$ star using the narrowband algorithm. The broadband algorithm was effective for stars as faint as $m_K = 14$. Fainter stars can be used if the integration time is increased. The second case involved a second channel sensor operating behind the PWFS. The purpose of the sensor is to detect jumps by an integer number of waves in the segment piston estimates. Running at 10 Hz and with only 10% of the light,

we can measure these jumps with an $m_I = 14$ star using narrowband light and the narrowband algorithm, or broadband light and the broadband algorithm.

## Acknowledgments

## REFERENCES

1. A. H. Bouchez *et al*, "The Giant Magellan telescope adaptive optics program," Proc. SPIE **9148**, 91480W (2014).

2. M. A. van Dam, B. A. McLeod and A. H. Bouchez, "A Dispersed Fringe Sensor for the Giant Magellan Telescope," *to appear in* Applied Optics (2016).

3. M. A. van Dam, B. A. McLeod and A. H. Bouchez, "Measuring Segment Piston with a Dispersed Fringe Sensor on the Giant Magellan Telescope," AO4ELT4, these proceedings (2016).

4. M. A. van Dam, *et al.*, "Design of a truth sensor for the GMT laser tomography adaptive optics system," Proc SPIE **8447**, 844717 (2012).

5. C. Verinaud, "On the nature of the measurements provided by a pyramid wave-front sensor," Optics Communications **233**, 27-38 (2004).

6. E. Pinna *et al*, "Design and numerical simulations of the GMT Natural Guide star WFS," Proc. SPIE **9148**, 91482M (2014).

7. A. C. Cheetham *et al.*, "Fizeau interferometric cophasing of segmented mirrors," Optics Express **20**, 29457-29471 (2012).

8. A. C. Cheetham *et al.*, "Fizeau interferometric cophasing of segmented mirrors: experimental validation," Optics Express **22**, 12924-12934 (2014).

9. R. Gerchberg and W. Saxton "A practical algorithm for the determination of phase from image and diffraction plane picture", Optik **35**, 237-246 (1972).

10. F. Rigaut and M. van Dam, "Simulating Astronomical Adaptive Optics Systems Using Yao," Proc. AO4ELT3, 18R (2013).

11. M. S. Goodwin, "Turbulence profiling at Siding Spring and Las Campanas Observatories," Ph.D. Thesis, Australian National University (2009).